Applied Physics A (2026) 132:148
https://doi.org/10.1007/s00339-026-09332-5

Applied Physics A
Materials Science & Processing

Enhancing solar energy harvesting through TiO_2-Fe_2O_3 composite photoanodes sensitized with natural dyes in photovoltaic cells

H. O. da Cunha[1] · A. M. B. Leite[1] · P. Sivasankaran[2] · R. Suresh Babu[1] · A. Kosiha[3] · A. L. F. de Barros[1]

Received: 15 October 2025 / Accepted: 12 January 2026

Abstract

This study investigated the enhancement of photovoltaic efficiency of dye-sensitized solar cells (DSSCs) through titanium dioxide (TiO_2) anodes composite with iron oxide (Fe_2O_3). TiO_2 with Fe_2O_3 at different weight percentages (0–30 wt%) were employed as photoanodes in DSSCs, prepared via mechanical mixing. Natural dyes extracted from *Chrysanthemum* violet and *Alstroemeria* flower petals were used as sensitizers, with platinum (Pt) cathode being employed to facilitate the photocatalytic process. The electronic excitation and molecule vibration characteristics of the dye molecules were investigated by UV-Vis and FTIR spectroscopy, respectively. For the analysis of the photovoltaic parameters, electrochemical characterizations were performed. The performances of the *Chrysanthemum* violet dye-sensitized cells with 10%, 20%, and 30% composite were 3.24%, 5.25%, and 4.15%, respectively, compared to 1.35% for the mere TiO_2 cells. Similarly, the photovoltaic conversion yields of the *Alstroemeria* dye-sensitized cells were 3.54%, 6.33%, and 5.74%, while the mere TiO_2 cells showed 1.74%. In both cases, composite with 20% Fe_2O_3 resulted in the highest efficiency. The findings indicate that this doping technique substantially improves the performance of DSSCs, reaching up to four times the efficiency compared to the mere TiO_2 cells. These results are promising and reinforce the potential of DSSCs in sustainable electricity production.

Keywords Dye-sensitized solar cells · Natural dyes · Photovoltaics · Renewable energy

1 Introduction

Dye-sensitized solar cells (DSSCs) represent an emerging photovoltaic technology that mimics the natural process of photosynthesis, offering a sustainable and cost-effective alternative for solar energy conversion [1]. A typical DSSC is composed of molecular dye adsorbed onto a porous semiconductor, usually titanium dioxide (TiO_2), which serves to harvest sunlight and generate electron-hole pairs [1, 2]. Upon light absorption, the excited electrons from the dye are injected into the conduction band of TiO_2 and subsequently transported through an external circuit to produce electricity [3]. The dye molecules are then regenerated by a redox electrolyte, ensuring the continuity of the process and contributing to the overall efficiency of the device [1–4].

Despite the advantages of TiO_2, including its high photoactivity and chemical stability, its application in DSSCs is limited by its wide bandgap, which restricts light absorption primarily to the UV region of the solar spectrum [5]. To address this limitation, doping strategies have been employed to modify the optical and electronic properties of TiO_2. Incorporation of metal oxides such as copper oxide (CuO) or iron oxide (Fe_2O_3) has shown promise in enhancing visible light absorption, tuning the bandgap, and reducing electron-hole recombination, thereby improving the overall efficiency of DSSCs [6–8]. Doping, therefore, emerges as a promising approach to overcome the inherent drawbacks of pure TiO_2-based photoanodes.

✉ H. O. da Cunha
higor.cunha@cefet-rj.br

✉ R. Suresh Babu
suresh.rajendran@aluno.cefet-rj.br

[1] Laboratory of Experimental and Applied Physics (LaFEA), Centro Federal de Educação Tecnológica Celso Suckow da Fonseca, Av. Maracanã 229, Rio de Janeiro 20271-110, Brazil

[2] Environmental and Climate Technology, Korea Institute of Energy Technology, 200 Hyeoksin-ro, Naju 58330, Republic of Korea

[3] Department of Chemistry, Vels Institute of Science, Technology & Advanced Studies, Chennai 600 117, India

Several metal complexes and organic dyes have been prepared and used as photosensitizers. So far, ruthenium based synthetic organic dyes are found to be effective sensitizers. By far, the highest efficiency of over 11% has been reported for DSSCs sensitized by Ru based dyes. However, the preparation methods for metal complexes are often based on multi-step process including tedious and expensive chromatographic purification methods. In parallel, the use of natural dyes derived from renewable sources has garnered significant interest due to their environmental benefits, low toxicity, and cost-effectiveness. It is anticipated that replacing synthetic organic dyes with natural pigments could resolve the above limitations as they can be easily extracted from the fruits, leaves, roots and flowers of plants. Natural pigments like anthocyanins, commonly found in fruits and flowers, possess strong light absorption capabilities and high affinity for metal oxide surfaces, making them ideal candidates for DSSC sensitizers [9–11]. Among these, extracts from flower petals such as *Chrysanthemum* and *Alstroemeria* are particularly notable due to the abundance of functional groups that facilitate efficient anchoring onto TiO_2 surfaces [12–18].

This study investigates the photovoltaic performance of DSSCs using Fe_2O_3 composite with TiO_2 photoanodes sensitized with natural dyes from *Chrysanthemum* and *Alstroemeria*. Composite with Fe_2O_3 (10–30 wt%) enhanced visible light absorption and charge separation, with 20% doping yielding optimal efficiency—up to four times higher than mere TiO_2 cells. Uniform TiO_2 films were prepared via spin coating, and dye interactions were analyzed using FTIR and UV–vis spectroscopy. Photovoltaic parameters were evaluated through current–voltage (*J–V*) and electrochemical impedance spectroscopy (EIS) measurements. The findings highlight the synergistic potential of semiconductor doping and natural dye sensitization, promoting a sustainable approach to high-efficiency DSSCs.

2 Experimental

2.1 Materials and methods

Fluorine-doped tin oxide (FTO)-coated conductive glass substrates (2.5 cm × 2.5 cm, surface resistivity~7 Ω/sq) were obtained from Sigma-Aldrich. Titanium dioxide (TiO_2) nanopowder (~21 nm), iron(III) oxide (Fe_2O_3, ~50 nm), polyethylene glycol (PEG), potassium iodide (KI), iodine (I_2), and hexachloroplatinic acid (H_2PtCl_2) were also sourced from Sigma-Aldrich. TEKBOND superglue, used for cell assembly, was purchased locally in Rio de Janeiro, Brazil.

Natural dyes were extracted from *Chrysanthemum* and *Alstroemeria* flower petals using an ethanol-based solvent system. The molecular structures and functional groups present in the dyes were analyzed using Fourier-transform infrared (FTIR) spectroscopy (Agilent Cary 630 FTIR). Light absorption properties in the UV–Vis range were studied using a SHIMADZU UV-2600i UV–Vis spectrophotometer. The band gap energy (Eg) of the samples was quantitatively estimated by Tauc equation using Kubelka–Munk function (Eq. 1):

$$(\mathrm{F}\ (\mathrm{R}) . \mathrm{h}\nu\ )\mathrm{n}\ =\ \mathrm{A}\,(\mathrm{h}\nu\ -\ \mathrm{Eg}) \tag{1}$$

Where F (R) is the Kubelka–Munk function, h is Planck's constant, ν is the frequency of incident light, A is a constant, Eg is the optical band gap, and n depends on the nature of the electronic transition (n = ½ for indirect band gap semiconductors such as TiO_2) [19].

Photovoltaic performance was evaluated using *J–V* and power–voltage (*P–V*) measurements under simulated sunlight (AM 1.5G, 100 mW/cm²) provided by an Ivisun® solar simulator (IVIUM Technologies). The fill factor (*FF*) was calculated using the following equation [20]:

$$FF = \frac{P_{max}}{J_{sc} . V_{oc}} \tag{2}$$

In order to evaluate the solar conversion performance of each DSSC, the photo-voltaic parameter is calculated through the efficiency (η), based on total incident power on the whole active cell area expressed by Eq. 3 [21].

$$\eta\ (\%) = \frac{J_{sc} . V_{oc} . FF}{P_{in}} . 100 \tag{3}$$

Electrochemical impedance spectroscopy was performed to analyze charge transport properties. All measurements were conducted using an IVIUM CompactStat multipotentiostat.

2.2 Extraction of natural dyes

Natural photosensitizers were extracted from the petals of *Chrysanthemum* and *Alstroemeria* flowers to explore their light-harvesting potential in DSSCs. Fresh petals (10 g) were first cleaned and then ground into a fine powder using a mortar and pestle. The powdered material was immersed in 100 mL of ethanol, selected for its effectiveness in dissolving pigment compounds while preserving their structural integrity. The mixture was stirred at room temperature to facilitate the extraction of dyed molecules. After sufficient contact time, the solution was filtered through standard filter paper to remove residual plant debris and particulates. The resulting clear dye solutions were stored in sterilized test tubes and refrigerated to prevent photodegradation and ensure stability prior to use in cell assembly.

2.3 Cathode preparation

Platinum was chosen as the counter electrode material due to its excellent catalytic activity, as demonstrated in prior studies [10, 11]. The counter electrode facilitates the reduction of oxidized species in the electrolyte, playing a crucial role in maintaining charge balance and enabling continuous current flow in DSSCs. FTO-coated glass substrates were used as the base for platinum deposition. Prior to catalyst application, the substrates were ultrasonicated in a 1:1 mixture of distilled water and ethanol for 20 min, followed by drying at 80 °C for 10 min. Surface conductivity was verified using a multimeter, yielding values between 10.3 and 12.5 Ω/sq. A 5 mM solution of hexachloroplatinic acid ($H_2PtCl_2 \cdot xH_2O$) in ethanol was prepared and applied to the cleaned substrates via drop-casting. The coated electrodes were then annealed at 350 °C for 30 min in a muffle furnace to promote adhesion and crystallinity of the platinum layer. After annealing, the samples were allowed to cool gradually to room temperature to minimize thermal stress and preserve film integrity.

2.4 Photoanode preparation

To ensure contamination-free conditions, all glassware was cleaned with distilled water, sterilized with ethanol, and dried at 90 °C for 10 min. For mere TiO_2 films, the precursor paste was prepared by mixing 1 g of TiO_2 nanopowder with 0.3 g of polyethylene glycol and 6 mL each of distilled water and acetic acid, followed by ultrasonication for 3 h to achieve uniform dispersion. For Fe_2O_3 composites, TiO_2 and Fe_2O_3 powders were first mechanically mixed in appropriate ratios to obtain doping levels of 10%, 20%, and 30% by weight. The iron oxide-TiO_2 mixture was then combined with 0.3 g of polyethylene glycol and 6 mL each of distilled water and acetic acid, followed by the same ultrasonication procedure to ensure a homogeneous dispersion. During all stages of TiO_2 handling, ambient lighting was minimized to prevent unwanted photoactivation. Thin films were deposited on FTO-coated glass substrates using a spin-coating technique at 1000 RPM for 10 s, controlled via Arduino software. The conductive side of each FTO substrate was confirmed with a multimeter prior to coating. Finally, the coated films were thermally annealed at 450 °C for 30 min in a muffle furnace to promote crystallinity and enhance electron transport. This treatment facilitated the anatase-to-rutile phase transformation of TiO_2, improving both light absorption and charge mobility within the photoanode layer.

2.5 Fabrication of DSSCs devices

Initially, the prepared TiO_2-Fe_2O_3 photoanodes were immersed in the natural dye extracts for 12 h at room temperature without ultrasonic treatment. Approximately 4 mL of each freshly filtered dye solution was used for complete submersion of the photoanode films. After immersion, the films were gently rinsed with ethanol to remove weakly bound molecules and dried at ambient conditions before cell assembly. Later, the dye-sensitized solar cells (DSSCs) were assembled by sandwiching the prepared photoanodes, previously sensitized with natural dyes extracted from *Chrysanthemum* and *Alstroemeria* petals with platinum-coated counter electrodes [10]. A spacer was placed between the electrodes to maintain a uniform gap, which was then filled with a redox electrolyte to facilitate ionic conduction. The electrolyte solution was prepared by dissolving 2.075 g of potassium iodide (KI), 0.12 g of iodine (I_2), and 0.2 g of polyethylene glycol in 5 mL of acetonitrile. This iodine-based redox couple (I^-/I_3^-) enables continuous electron cycling between the photoanode and cathode. During assembly, care was taken to avoid electrolyte leakage beyond the active area, which could adversely affect device performance. To seal the cell, a small amount of superglue was applied externally along two adjacent edges of one electrode in a parallel configuration, leaving the remaining edges open for electrical contact. This sealing ensured mechanical stability without interfering with electrochemical properties. A schematic illustration of the assembled DSSC is provided in Scheme 1, highlighting the configuration and spatial arrangement of all key components.

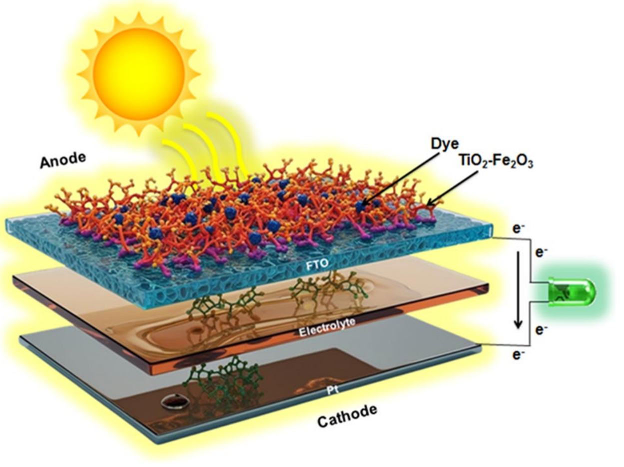

Scheme 1 DSSC assembly diagram

3 Results and discussion

3.1 X-ray diffraction

The phase composition and crystalline structure of the synthesized TiO_2-Fe_2O_3 composites were investigated using X-ray diffraction (XRD), as presented in Fig. 1. The XRD pattern includes pristine TiO_2 and TiO_2-Fe_2O_3 composites with varying Fe_2O_3 contents (10 wt %, 20 wt %, and 30 wt %). The XRD pattern of pristine TiO_2 shows characteristic peaks corresponding to both the anatase (JCPDS No. 21–1272) and rutile (JCPDS No. 21–1276) phases [22, 23]. The dominant diffraction peaks at $2\theta \approx 25.3°$, 37.8°, 48.0°, and 54.0° correspond to the (101), (004), (200), and (105) planes of anatase TiO_2, while additional peaks are from rutile phase. The presence of multiple TiO_2 phases indicates a mixed-phase structure in the pristine sample. When making composite with Fe_2O_3 from 10 wt % to 30 wt %, new diffraction peaks emerge that match the hematite phase (α-Fe_2O_3) based on JCPDS No. 33–0664 [24, 25]. These peaks become more prominent with increasing Fe_2O_3 content, indicating the progressive incorporation of Fe_2O_3 into the composite structure. The zoomed X-ray diffraction curves were presented in Figure S1 (see supporting information). Importantly, the following two observations are evident: (i) A systematic shift in the diffraction peaks of anatase TiO_2 is observed with increasing Fe_2O_3 loading. This peak shift suggests a possible lattice distortion due to the substitution of Ti^{4+} by Fe^{3+} ions or the formation of strain at the TiO_2-Fe_2O_3 interface. Such structural modifications imply an interaction at the atomic level, which may promote better charge separation and transport-properties highly desirable for electrochemical applications. (ii) The intensity of the main anatase TiO_2 peaks gradually decreases as the Fe_2O_3 content increases from 10 wt% to 30 wt%. This decrease in crystalline could be due to several factors: the introduction of structural disorder, partial amorphization of TiO_2, or increased surface coverage by Fe_2O_3 nanoparticles. The reduced intensity implies a lower degree of long-range order, potentially leading to more active sites and surface defects, which can enhance charge storage behavior. Together, the XRD results confirm the successful formation of TiO_2–Fe_2O_3 composites and indicate that increasing Fe_2O_3 content significantly influences the structural characteristics of the material. The observed peak shift and reduced diffraction peaks indicates the strong interaction between TiO_2 and Fe_2O_3, which could be critical in tuning the electrochemical or photocatalytic performance of the composites. Moreover, Fig. 2 shows the crystal structure of Anatase TiO_2, Rutile TiO_2 and Fe_2O_3 phases. Anatase TiO_2 is beta Vanadium nitride-like structured and crystallizes in the tetragonal $I4_1/amd$ space group. Ti^{4+} is bonded to six equivalent O^{2-} atoms to form a mixture of distorted corner and edge-sharing TiO_6 octahedra. The corner-sharing octahedral tilt angles are 25°. There are four shorter (1.94 Å) and two longer (1.99 Å) Ti-O bond lengths. O^{2-} is bonded in a distorted T-shaped geometry to three equivalent Ti^{4+} atoms. TiO_2 is Rutile structured and crystallizes in the tetragonal $P4_2/mnm$ space group. Ti^{4+} is bonded to six equivalent O^{2-} atoms to form a mixture of corner and edge-sharing TiO_6 octahedra. The corner-sharing octahedral tilt angles are 49°. There are four shorter (1.95 Å) and two longer (1.98 Å) Ti-O bond lengths. O^{2-} is bonded in a distorted trigonal planar geometry to three equivalent Ti^{4+} atoms. Fe_2O_3 is Corundum structured and crystallizes in the trigonal $R\bar{3}c$ space group. Fe^{3+} is bonded to six equivalent O^{2-} atoms to form a mixture of distorted corner, edge, and face-sharing FeO_6 octahedra. The corner-sharing octahedral tilt angles range from 48–61°. There are three shorter (1.97 Å) and three longer (2.12 Å) Fe-O bond lengths. O^{2-} is bonded to four equivalent Fe^{3+} atoms to form a mixture of distorted corner and edge-sharing OFe_4 trigonal pyramids.

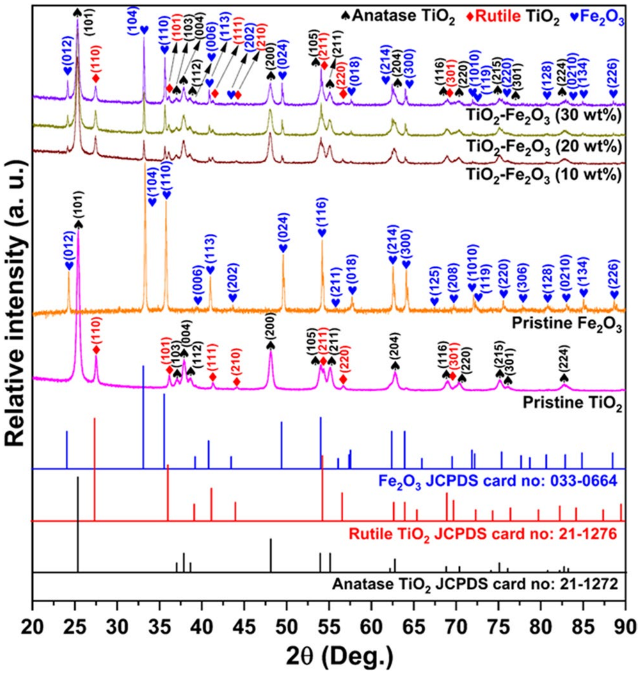

Fig. 1 XRD patterns of TiO_2 and various percentages of TiO_2-Fe_2O_3 composites

3.2 UV-Vis diffuse reflectance spectroscopy (DRS UV-Vis)

The optical properties of as-synthesized photocatalysts were investigated using UV-Vis DRS, and the corresponding spectra are shown in Fig. 3a. As depicted in Fig. 3a, pristine TiO_2, pristine Fe_2O_3 and the TiO_2–Fe_2O_3 composite samples exhibit prominent absorption in the ultraviolet (UV) region, a characteristic feature of TiO_2 due to its wide band gap of

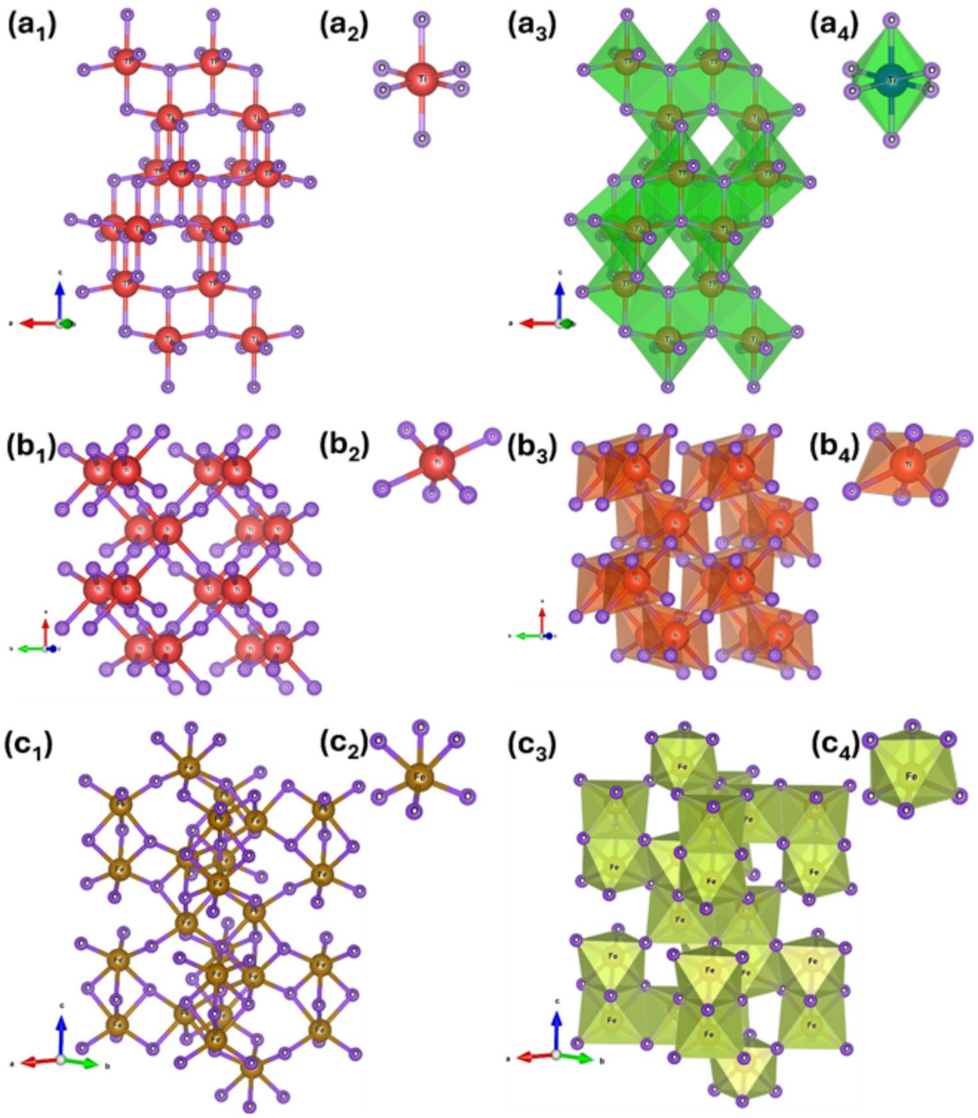

Fig. 2 The crystal structures of tetragonal Anatase TiO_2, tetragonal Rutile TiO_2 and rhombohedral (or) trigonal Fe_2O_3 drawn by Vesta software (Version 3.4.5). (**a**$_1$) Ball-and-stick model of Anatase TiO_2 crystal structure and (**a**$_2$) their corresponding single unit cell, (**a**$_3$) polyhedral model of Anatase TiO_2 crystal structure and (**a**$_4$) their corresponding single unit cell. (**b**$_1$) Ball-and-stick model of Rutile TiO_2 crystal structure and (**b**$_2$) their corresponding single unit cell, (**b**$_3$) polyhedral model of Rutile TiO_2 crystal structure and (**b**$_4$) their corresponding single unit cell. (**c**$_1$) Ball-and-stick model of Fe_2O_3 crystal structure (**c**$_2$) their corresponding single unit cell (**c**$_3$) polyhedral model of Fe_2O_3 crystal structure and (**c**$_4$) their corresponding single unit cell

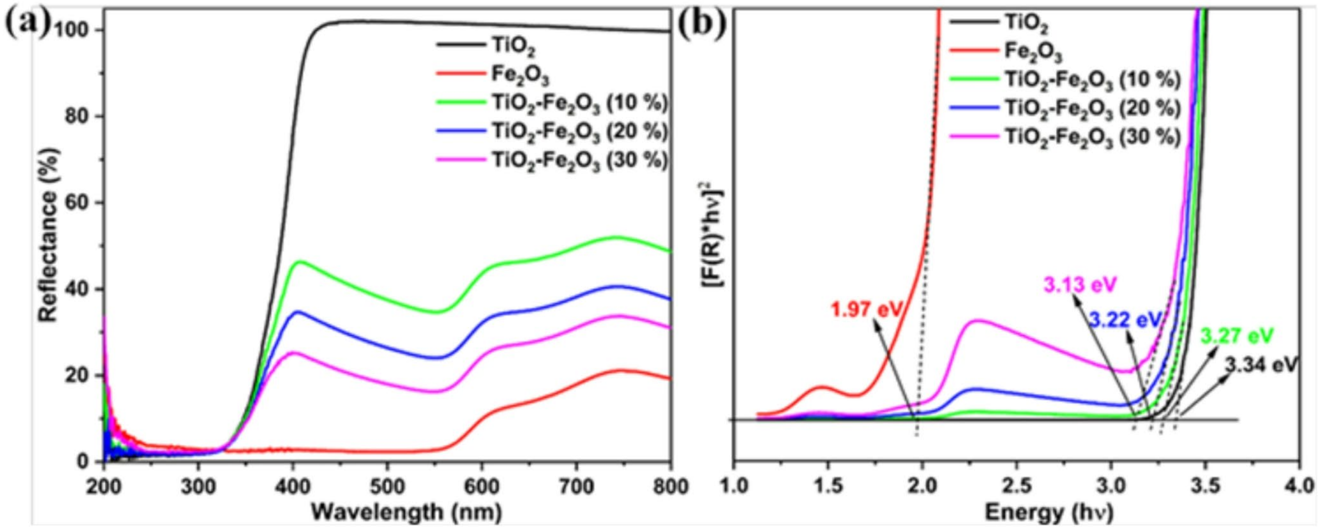

Fig. 3 (**a**) UV-Vis diffuse reflectance spectra (DRS) of pristine TiO_2, pristine Fe_2O_3 and TiO_2-Fe_2O_3 (10, 20 and 30% wt %). (**b**) Corresponding Tauc plot used to estimate the optical band gaps. The progressive redshift and band-gap narrowing with increasing Fe_2O_3 content are highlighted

3.34 eV. This confirms that TiO_2 is predominantly active under UV light irradiation. However, upon incorporation of Fe_2O_3, which has a narrower band gap of approximately 1.97 eV, a redshift in the absorption edge is observed for the TiO_2–Fe_2O_3 composites (Fig. 3b). This shift indicates enhanced visible light absorption with increasing Fe_2O_3 content, attributed to the formation of an intimate interfacial contact between TiO_2 and Fe_2O_3, which facilitates better charge separation and utilization of the solar spectrum. Although Fe_2O_3 incorporation introduces strong absorption in the visible range due to intra-d orbital transitions and charge-transfer effects, these features do not correspond to direct interband transitions. Therefore, for accurate estimation of the composite bandgap, we focused on the absorption onset corresponding to indirect allowed transitions, consistent with anatase TiO_2. The progressive redshift observed with increasing Fe_2O_3 content is attributed to interfacial charge transfer, orbital coupling, and local band bending, which effectively modulate the TiO_2 band structure and enhance visible light absorption without fundamentally altering the host semiconductor's transition type.

Figure 3b presents the Tauc plots for the pristine TiO_2 and TiO_2–Fe_2O_3 composite samples and composite samples. The band gap of pristine TiO_2 was calculated to be 3.34 eV, consistent with literature values [26–28]. Upon incorporating Fe_2O_3, the band gaps of the TiO_2–Fe_2O_3 composites gradually decreased with increasing Fe_2O_3 content: 3.27 eV for TiO_2–Fe_2O_3 (10%), 3.22 eV for TiO_2–Fe_2O_3 (20%), and 3.13 eV for TiO_2–Fe_2O_3 (30%). This progressive band gap narrowing suggests improved absorption of visible light, which is advantageous for photocatalytic applications under solar irradiation. The observed redshift and band gap reduction can be attributed to the electronic interaction between TiO_2 and Fe_2O_3, leading to the formation of band bending at the electrode-electrolyte interface, which modifies the optical transitions. These results confirm the successful modification of TiO_2 optical properties through Fe_2O_3 incorporation, potentially enhancing photocatalytic efficiency under visible light.

.

3.3 FT-IR and UV-Vis spectroscopy of dye analysis

The FTIR spectra of natural dyes extracted from *Chrysanthemum* and *Alstroemeria* petals (Fig. 4a) reveal key functional groups relevant to their role in dye-sensitized solar cells (DSSCs). A broad absorption band between 3100 and 3500 cm^{-1} corresponds to O–H stretching vibrations, indicative of hydroxyl groups commonly present in natural organic dyes [12]. Peaks observed between 2850 and 3000 cm^{-1} are attributed to symmetric and asymmetric C–H stretching modes within aliphatic and aromatic structures [13]. In particular, peaks in the region of 1650–1750 cm^{-1} are assigned to C=C stretching vibrations, suggesting the presence of conjugated double bonds, typically associated with aromatic or alkene groups. An additional prominent band between 1000 and 1250 cm^{-1} is attributed to C=O stretching vibrations, confirming the presence of carbonyl groups [12, 13]. These carbonyl and hydroxyl functionalities are critical for dye–semiconductor interactions. Specifically, carbonyl groups facilitate anchoring of the dye molecules onto the TiO_2 surface via coordination bonds, enhancing electron injection from the excited dye into the conduction band of TiO_2. This molecular interaction plays a pivot-al role in initiating the photoinduced charge separation and overall photovoltaic performance of the DSSC.

UV-vis spectroscopy is a key analytical technique for evaluating the optical properties of dyes used in dye-sensitized solar cells (DSSCs). It offers insight into the dyes' light absorption capacity and their suitability as photosensitizers. Figures 4b and **c** shows the UV-vis absorption spectra of the natural dyes extracted from *Alstroemeria* and *Chrysanthemum* petals. Both dyes exhibit a broad absorption band in the near-UV region, ranging from approximately 283 to 331 nm. This region corresponds to the $\pi \rightarrow \pi^*$ electronic transitions, commonly associated with anthocyanin pigments-particularly petunidin-based radicals-responsible for the vibrant coloration of these flowers [12, 13]. The absorption in this region is advantageous, as it partially overlaps with the solar spectrum, thereby enhancing the dyes' light-harvesting efficiency. The strong UV absorption suggests that these natural dyes possess the potential to function as effective sensitizers in DSSCs by enabling efficient photon capture and promoting electron excitation, which are essential for subsequent injection into the semiconductor conduction band.

3.4 Morphological analysis using atomic force microscopy

Atomic force microscopy (AFM) was performed to analyze the surface morphol-ogy and topography of TiO_2 photoanodes sensitized with natural dyes *Alstroemeria* (ALS) and *Chrysanthemum* violet (C.V.) and varying concentrations of Fe_2O_3 in TiO_2 composites. The three-dimensional AFM images shown in Fig. 5 provide insights into how both Fe_2O_3 doping and the nature of the bio-photosensitizer influence surface characteristics, which directly affect dye loading capacity and charge transport efficiency in dye-sensitized solar cells (DSSCs). Figure 5(a) shows the mere TiO_2 pho-to anode sensitized with Alstroemeria extract (ALS), featuring a relatively smooth sur-face with minor irregularities [29], and potentially limiting dye adsorption. With 10% Fe_2O_3 doping [Figure 5(b)], the surface becomes more textured,

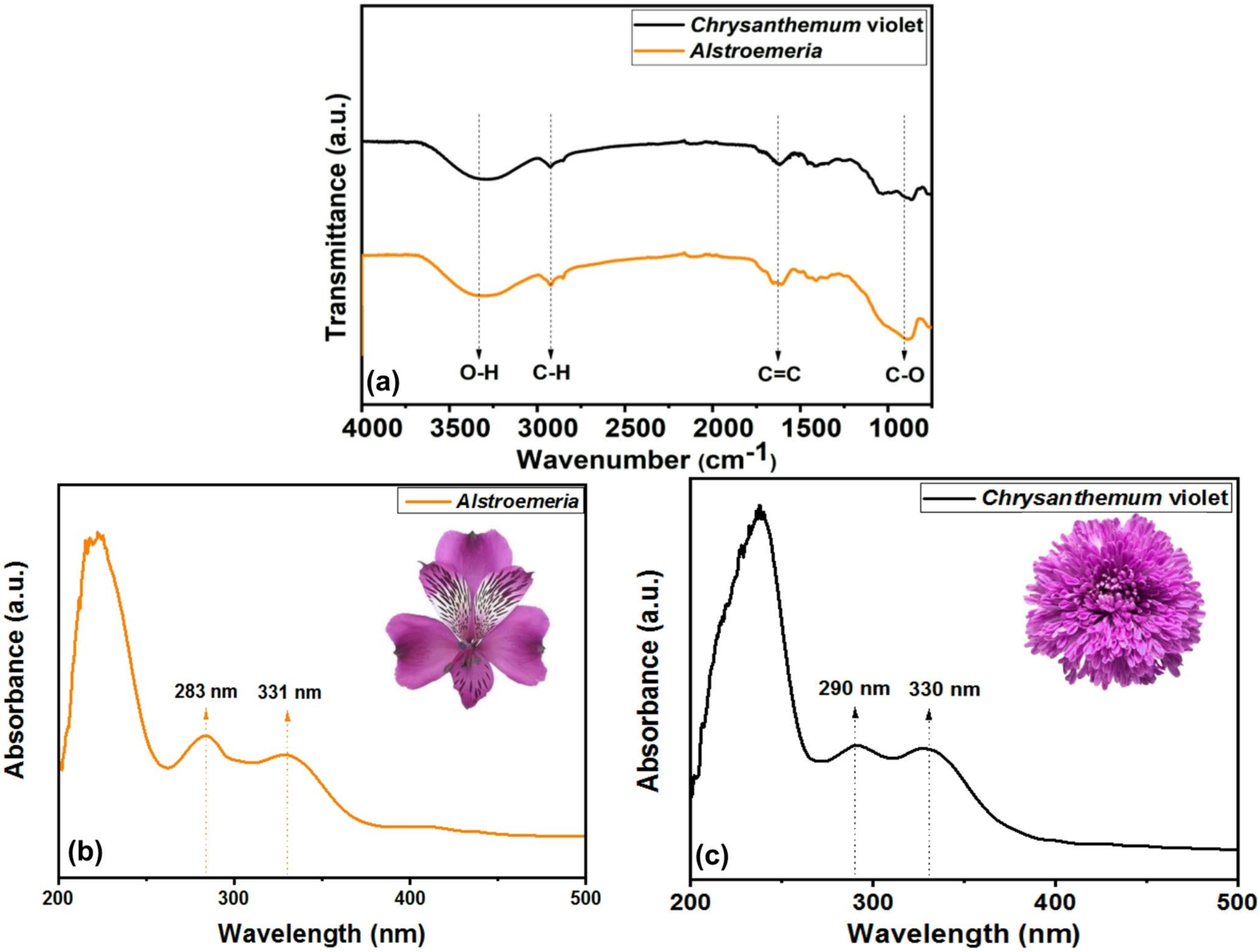

Fig. 4 (**a**) FTIR spectra of dyes extracted from *Alstroemeria* and *Chrysanthemum* violet. UV-Vis absorption spectra of the extracted dyes from (**b**) *Alstroemeria* and (**c**) *Chrysanthemum* violet

showing the formation of finer grains and increased porosity. At 20% doping [Figure 5(c)], the ALS-sensitized photoanode displays an optimal porous network with well-distributed and larger grain structures. This morphology enhances the effective surface area, which is favorable for dye adsorption and facilitates better electron mobility. However, increasing the Fe_2O_3 concentration to 30% [Figure 5(d)] results in a denser and less porous structure, likely due to excess dopant aggregation. This reduced porosity can obstruct dye infiltration and impede electron diffusion [30, 31], ultimately degrading device performance. A similar trend is observed in TiO_2 photoanodes sensitized with Chrysanthemum violet (C.V.) [Figures 5(e)–5(h)]. The mere TiO_2-C.V. film [Figure 5(e)] has a smoother surface, while 10% and 20% Fe_2O_3 doping [Figures 5(f) and 5(g)] introduce a more favorable grain texture and porosity. Among them, the 20% Fe_2O_3-C.V. sample [Figure 5(g)] exhibits the most uniform and porous surface, ideal for enhanced dye interaction and improved electron transport. In contrast, 30% doping [Figure 5(h)] again results in morphological deterioration, indicating a saturation point beyond which further doping becomes counterproductive. Additionally, Fig. 5(i) shows the AFM image of the platinum-coated counter electrode prepared by drop casting. The image confirms a uniform distribution of platinum particles across the FTO surface, ensuring efficient electrocatalytic activity for the redox couple in the electrolyte. In conclusion, AFM analysis reveals that both Fe_2O_3 concentration and the type of natural dye sensitizer significantly affect surface morphology. The 20% Fe_2O_3-TiO_2 photoanodes sensitized with either Alstroemeria or Chrysanthemum violet exhibit the most favorable topography for enhanced dye loading and electron transport, making them promising candi-dates for high-performance DSSCs.

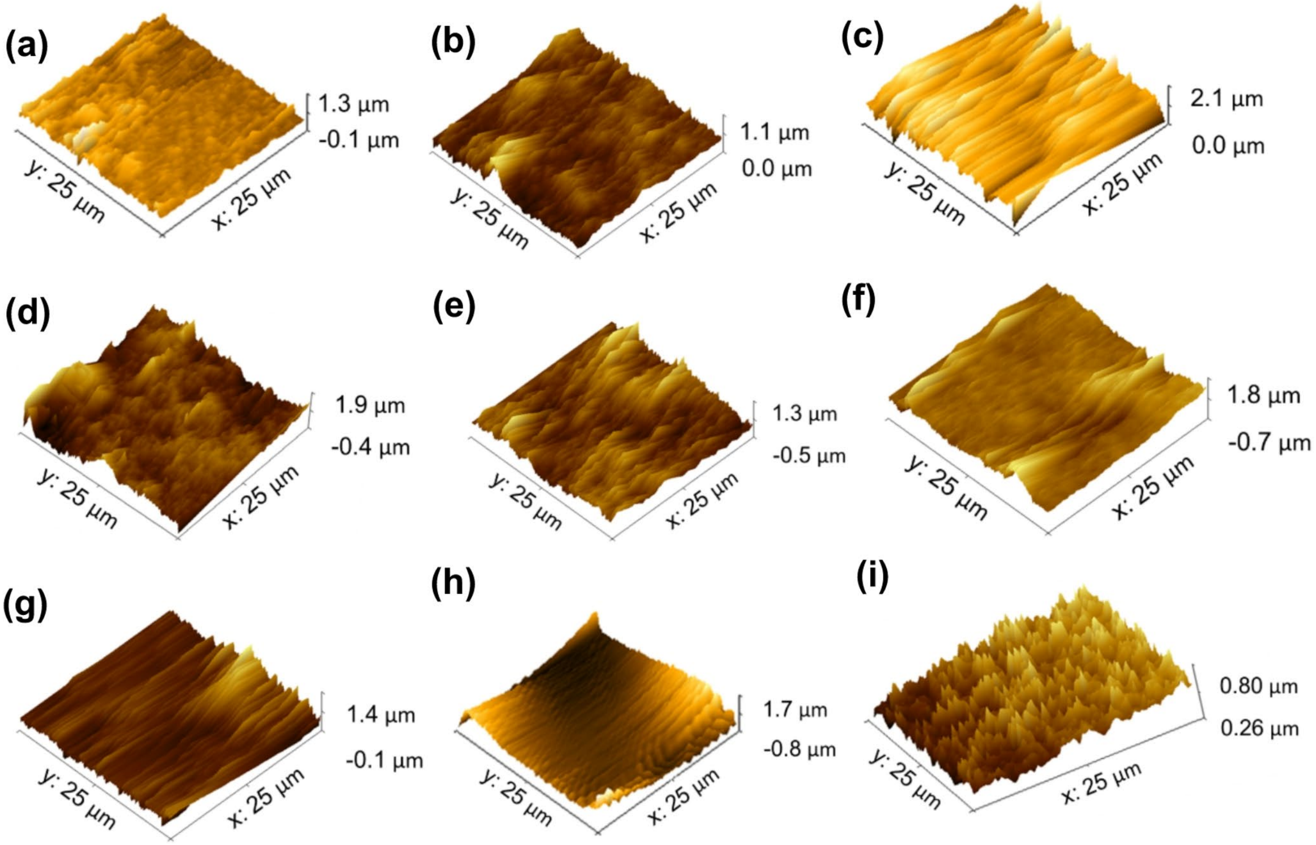

Fig. 5 Three-dimensional AFM images: photoanodes such as (**a**) TiO_2 (ALS), (**b**) TiO_2-Fe_2O_3(10%) (ALS), (**c**) TiO_2-Fe_2O_3(20%) (ALS), (**d**) TiO_2-Fe_2O_3(30%) (ALS), (**e**) TiO_2 (C.V.), (f) TiO_2-Fe_2O_3(10%) (C.V.), (**g**) TiO_2-Fe_2O_3(20%) (C.V.), (**h**) TiO_2- Fe_2O_3(30%) (C.V.). (**i**) Pt cathode

3.5 Electrochemical studies for dye-sensitized solar cells (DSSCs)

Electrochemical characterization is crucial for understanding the internal mechanisms of dye-sensitized solar cells (DSSCs) and identifying factors that affect their efficiency [32]. The current-voltage (*I–V*) curve provides essential parameters such as short-circuit current density (J_{sc}), open-circuit voltage (V_{oc}), fill factor (FF), and overall photovoltaic conversion efficiency (η) [33]. Figures 6a and b shows the *I–V* curves of DSSCs sensitized with *Alstroemeria* (Als) and *Chrysanthemum violet* (C.V.) dyes, incorporating different concentrations of Fe_2O_3 dopant.

The short-circuit current density (J_{sc}), a key indicator of photoresponse, increased with Fe_2O_3 doping up to 20%, reaching 3.91 mA/cm² for Als and 2.71 mA/cm² for C.V. A slight decline was observed at 30% doping (3.48 mA/cm² and 2.42 mA/cm², respectively), though these values remained higher than those obtained with pure TiO_2 (2.04 mA/cm² for Als and 0.84 mA/cm² for C.V.) and 10% doping (2.48 mA/cm² and 2.36 mA/cm², respectively) [34, 35]. In addition to the *I–V* characterization, the power–voltage (*P–V*) curves shown in Figs. 6c and d provide insights into the operating performance of the cells [36–39]. The highest power outputs—1.01 mW/cm² (Als) and 0.84 mW/cm² (C.V.)—were also recorded at 20% Fe_2O_3 doping, consistent with the trends in current density. Finally, the fill factor (FF) and the conversion efficiency (η), were calculated using the above Eqs. (2) and (3).

The working principle of the DSSC employing a TiO_2-Fe_2O_3 nanocomposite photoanode under solar illumination is illustrated in Fig. 7. Based on functional group analysis and literature precedent, the natural dye molecules are expected to preferentially bind to surface hydroxyl groups on TiO_2 nanoparticles via coordination with carbonyl and hydroxyl functionalities. Binding to Fe_2O_3 may be secondary or limited due to fewer accessible surface-active sites and lower surface hydroxylation under comparable conditions. Prior to forming a heterojunction (Before contact), the Fermi level (Ef) of Fe_2O_3 lies at a lower energy compared to that of TiO_2 due to the intrinsic difference in their electronic structures. Simultaneously, the conduction band (CB) and valence band (VB) edges of Fe_2O_3 are energetically situated in a straddling configuration relative to those of TiO_2 which means that both the CB and VB of Fe_2O_3 lie within the corresponding energy range of TiO_2 as shown in Fig. 7a. Upon

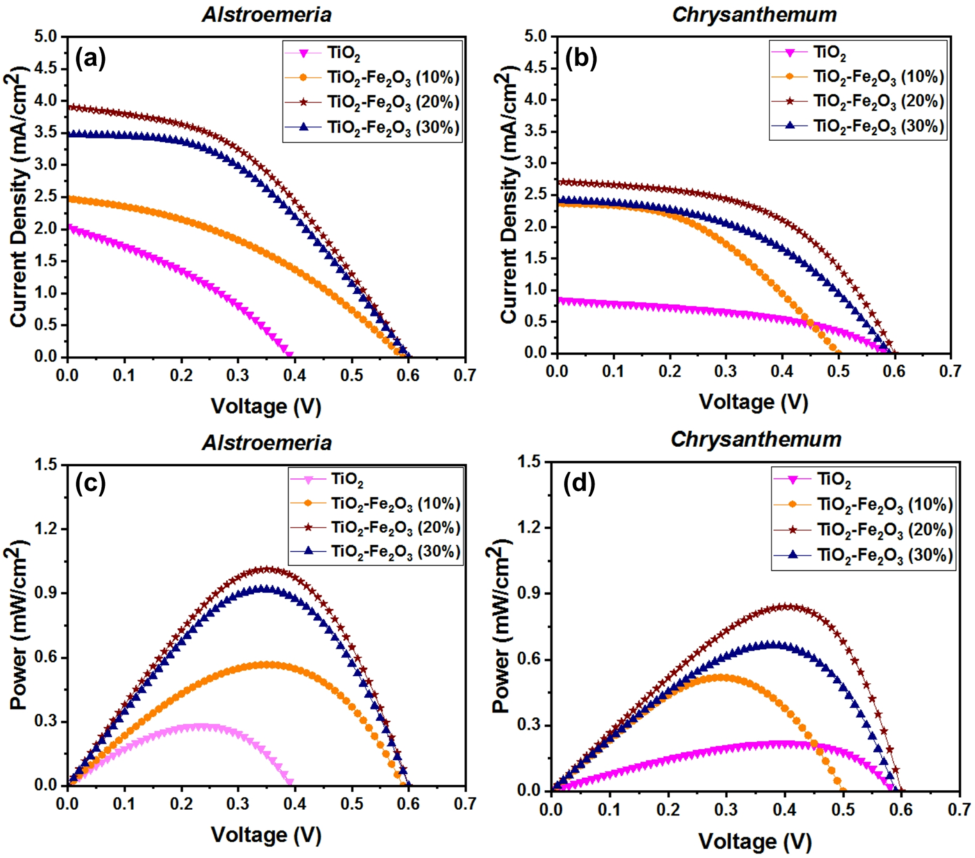

Fig. 6 Current density curves (J_{sc}) with the various composites: (**a**) *Alstroemeria* and (**b**) *Chrysanthemum violet*. PV curves with the various composites: (**c**) *Alstroemeria* and (**d**) *Chrysanthemum violet*

intimate interfacial contact between the two semiconductors (After contact), a heterojunction is formed, and the system reaches thermodynamic equilibrium through Fermi level alignment. This equilibration process involves interfacial charge redistribution, resulting in an upward shift of the CB edge of Fe_2O_3 relative to that of TiO_2 as shown in Fig. 7b. Consequently, an internal electric field is established at the interface, oriented from TiO_2 toward Fe_2O_3. This built-in electric field plays a critical role in directing charge carrier dynamics. Under illumination, photogenerated electrons in the CB of Fe_2O_3 are energetically driven to migrate toward the CB of TiO_2, facilitated by the favorable band alignment. In parallel, photogenerated holes in TiO_2 are pushed in the opposite direction, migrating into the VB of Fe_2O_3. This spatial separation of charge carriers across the heterointerface significantly suppresses recombination and promotes efficient charge utilization, which is essential for enhancing solar cell performance.

Upon light irradiation, the dye molecules (*Chrysanthemum* and *Alstroemeria*), adsorbed onto the surface of the photoanode, absorb photons and undergo photoexcitation. The excited electrons from the dye molecules are subsequently injected into the conduction band (CB) of Fe_2O_3 and then transferred to the CB of TiO_2, facilitating directional charge transport toward the fluorine-doped tin oxide (FTO) substrate. Following electron injection, the oxidized dye molecules (Dye^+) are regenerated by electron donation from the redox electrolyte (typically I^-/I_3^-). This regenerative cycle is completed at the platinum counter electrode, where electrons arriving through the external circuit reduce I_3^- back to I^-, thus sustaining continuous photocurrent generation (Fig. 7c). The introduction of Fe_2O_3 into the TiO_2 matrix plays multiple functional roles. Firstly, Fe_2O_3, with a narrower band gap (~ 1.97 eV), extends the optical absorption into the visible region, thereby enhancing solar light harvesting. Secondly, Fe_2O_3 acts as an efficient electron mediator or sink, promoting interfacial charge separation and transfer, and suppressing recombination by retarding electron backflow to the oxidized species in the electrolyte. Additionally, Fe_2O_3 nanoparticles contribute to localized light trapping via plasmonic-like scattering effects, which intensify the local electromagnetic field and increase the effective optical path length. This coupling with dye molecules enhances dye absorption, leading to a substantial increase in photocurrent density, as evidenced in the *J–V* characteristics. Overall, the TiO_2-Fe_2O_3 nanocomposite photoanode satisfies key criteria for efficient photovoltaic performances improved light harvesting, effective charge separation, and reduced recombination thereby

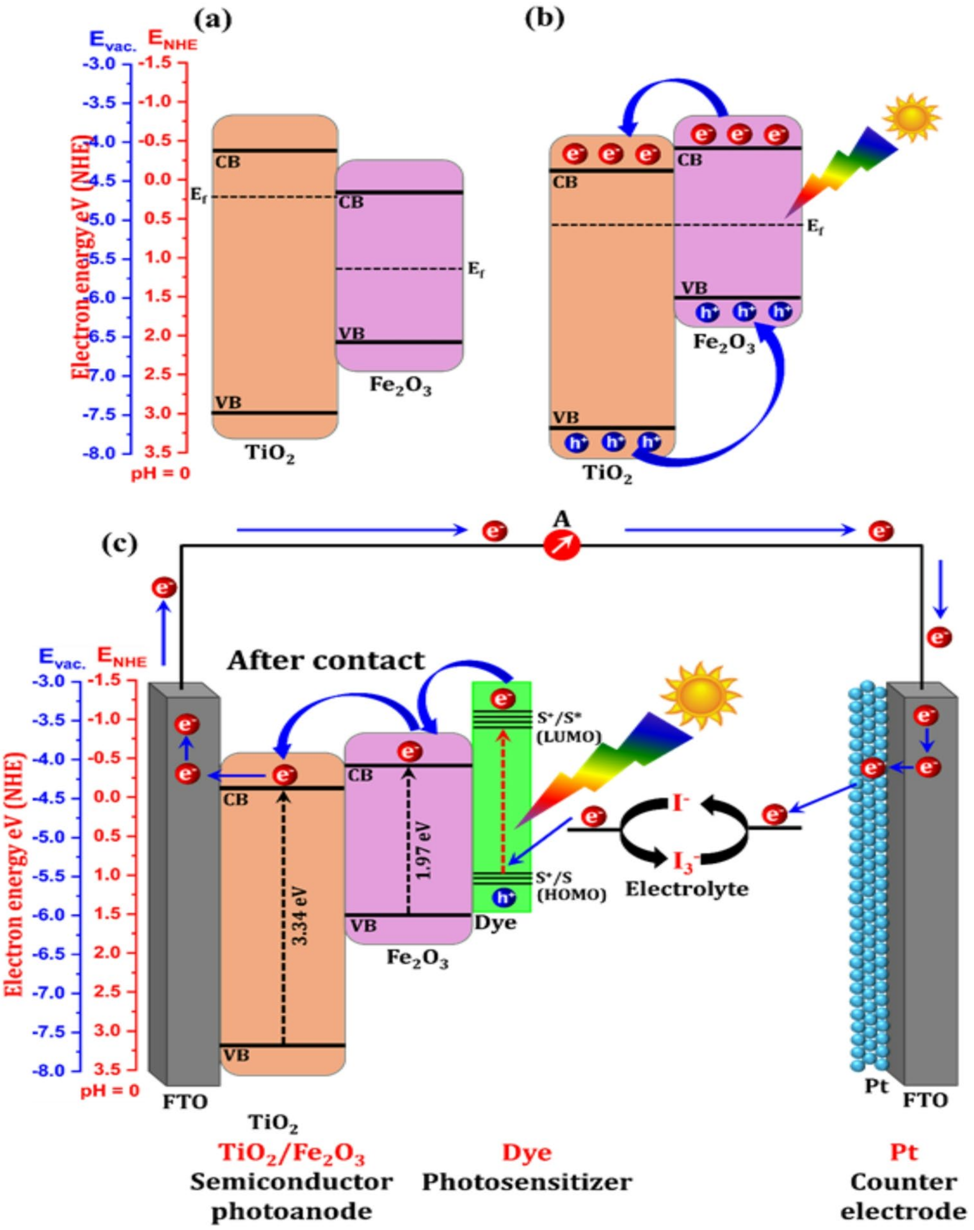

Fig. 7 Schematic illustration of the valence band (VB) and conduction band (CB) positions of TiO_2-Fe_2O_3 nanocomposite photoanode (**a**) before contact and (**b**) after contact. (**c**) Electron transfer mechanism across the energy levels in the TiO_2–Fe_2O_3 nanocomposite photoanode under light irradiation

demonstrating its potential as a high-performance photoanode architecture for next-generation DSSCs.

Figure 8 shows the mentioned photovoltaic parameters (V_{oc}, J_{sc}, *FF* and P_{max}). The current density was limited by the rapid recombination of charge carriers due to the absence of dopants. For ALS-TiO_2 and C.V.-TiO_2, the J_{sc} values were 2.04 mA/cm² and 0.85 mA/cm², respectively. Doping at 10% Fe_2O_3 improved charge transport, raising J_{sc} to 2.48 mA/cm² (ALS) and 2.37 mA/cm² (C.V.). This is due to the introduction of intermediate states that facilitate light capture. Doping at 20% Fe_2O_3 showed the best performance, with J_{sc} reaching 3.91 mA/cm² (ALS) and 2.71 mA/cm² (C.V.). With 30% Fe_2O_3 doping, there was a drop in values to 3.48 mA/cm² (ALS) and 2.42 mA/cm² (C.V.), indicating saturation and increased recombination. With only TiO_2, V_{oc} was limited by low charge separation efficiency, with values of 0.39 V (ALS) and 0.58 V (C.V.). Doping with Fe_2O_3 increased V_{oc} in all proportions due to reduced recombination and better energy level alignment [40]. Doping at 20% stood out, reaching a V_{oc} of 0.60 V for both dyes, the maximum value observed. With pure TiO_2, the *FF* presented low values, with 0.29 (ALS) and 0.44 (C.V.), reflecting resistive losses and low stability of the charge carriers. At 10% and 20% doping, the *FF* increased progressively, reaching 0.43 (ALS) and 0.52 (C.V.) for the 20% doping. At 30% doping, there was a slight decrease to 0.44 (ALS) and 0.46 (C.V.), probably due to the excess of dopants, which impaired

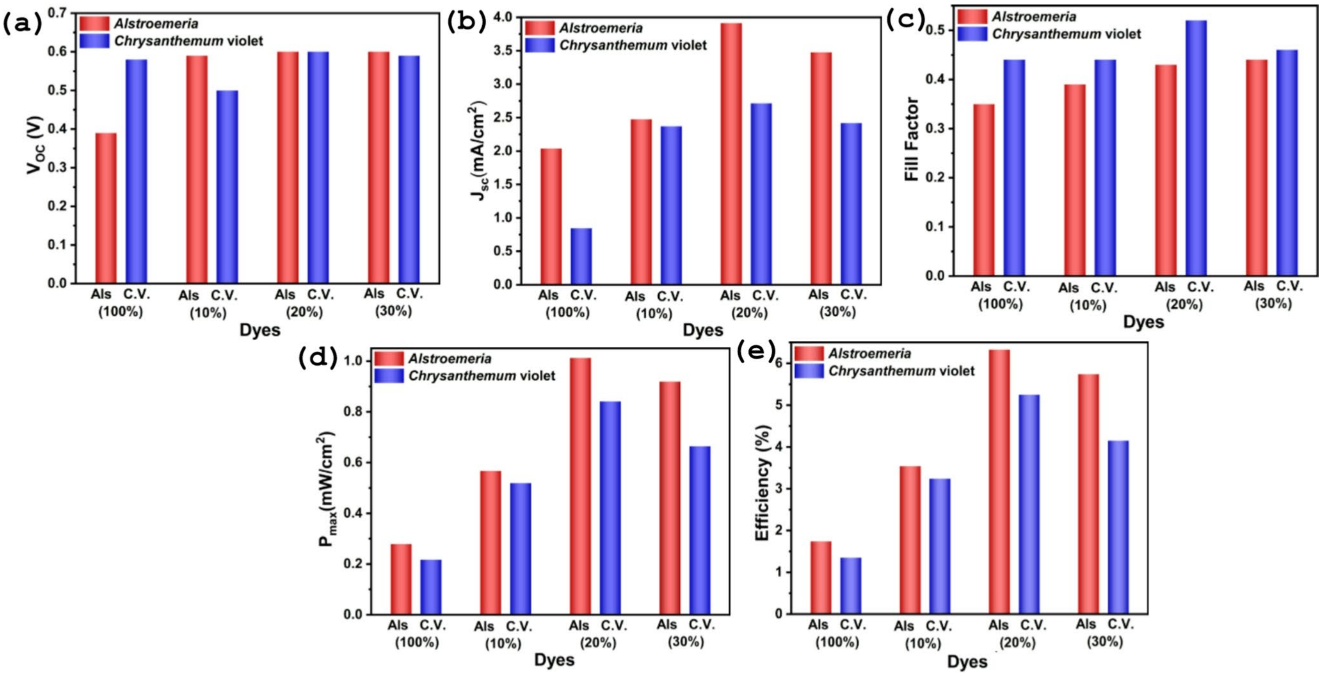

Fig. 8 Photovoltaic parameters of TiO_2 and various percentages of TiO_2-Fe_2O_3 composites photoanodes with *Alstroemeria* and *Chrysanthemum* violet dyes: (a) V_{oc}, (b) J_{sc}, (c) FF, (d) P_{max} and (e) η

the electronic conductivity [41]. The solar conversion performance of each DSSC is shown in Fig. 8e. Pure TiO_2 showed the lowest efficiencies recorded, with 1.74% (ALS) and 1.35% (C.V.). At 10% doping, the efficiency increased to 3.54% (ALS) and 3.24% (C.V.). At 20% doping, the best result was observed under this condition, with η of 6.33% (ALS) and 5.25% (C.V.), due to the ideal balance between charge transport and light absorption. At 30% doping, there was a reduction to 5.74% (ALS) and 4.15% (C.V.), indicating saturation and compromised efficiency. The optimized TiO_2-Fe_2O_3/natural dye photoanode developed here is directly applicable to low-cost, environmentally friendly DSSCs with improved visible-light harvesting and charge-transfer performance. The enhanced efficiency achieved using renewable floral dyes and a stable TiO_2-Fe_2O_3 heterojunction highlights its potential for sustainable photovoltaic devices, portable power sources, and small-scale renewable energy systems. Table 1 presents the comparison of the photovoltaic parameters of DSSCs using only TiO_2 anodes and those composites with Fe_2O_3 sensitized with different natural dyes obtained in this work with those in the literature [12–18, 42–44].

Electrochemical impedance spectroscopy (EIS) was conducted to further evaluate the charge transport and recombination dynamics within the DSSCs. Figures 9(a) and 9(b) display the Nyquist plots, and Fig. 9(c) presents the equivalent circuit model. The corresponding impedance parameters and their errors are summarized in Table 2. At higher frequencies, the small semicircle is attributed to the charge transfer resistance (R_1) arising from the redox electrolyte and the Pt counter electrode (electrolyte/Pt interface). In the lower frequency region, the larger semicircle corresponds to the resistance associated with charge transport across the dye-adsorbed TiO_2/electrolyte interface (R_2). The solution resistance (R_s) represents the combined resistance of the electrolyte and the FTO substrate, while R_3 is related to electrolyte diffusion and the series ohmic resistance. The largest semicircles, indicative of higher charge-transfer resistance, were observed in the mere TiO_2 cells, while 20% Fe_2O_3 doping resulted in the smallest semicircles, confirming improved charge transport and reduced internal resistance [32].

The long-term operational stability of DSSCs remains a critical factor in their pathway toward commercialization. To evaluate the durability of the fabricated cells, a six-month stability study was conducted under ambient storage conditions. The results (Table 3) indicate that the devices retained a significant portion of their initial power conversion efficiency throughout the testing period, with only a gradual decline observed over time. This performance retention demonstrates that the fabricated DSSCs, despite the known limitations of organic pigments, exhibit reasonable stability within the investigated timeframe. These findings suggest that appropriate encapsulation strategies and electrolyte optimization could further extend device lifetime, thereby supporting the practical applicability of *Alstroemeria* and *Chrysanthemum*-based DSSCs.

Table 1 Photovoltaic parameters using TiO_2-Fe_2O_3 composite anodes sensitized with different natural dyes

Dyes	Anode	J_{sc} (mA/cm^2)	V_{oc} (V)	*FF*	η (%)	Ref.
Annona atemoya	TiO_2	0.06	0.50	0.62	0.19	[14]
Physalis peruviana	TiO_2	0.30	0.39	0.42	0.30	[14]
Lantana repens	TiO_2	0.45	0.69	0.34	0.12	[15]
Solidago canadensis	TiO_2	0.93	0.79	0.42	0.31	[15]
Gerbera	TiO_2	1.22	0.59	0.53	1.54	[16]
Leucanthemum	TiO_2	0.42	0.54	0.27	0.88	[17]
Pawpaw	TiO_2	5.10	0.49	0.30	1.72	[18]
Pawpaw	TiO_2-Fe_3O_4	6.10	0.72	0.33	3.28	[18]
Ocimum gratissimum	TiO_2	0.07	0.26	0.36	1.70	[37]
Ocimum gratissimum	TiO_2-FeO	0.10	0.43	0.46	4.00	[37]
Black grape	TiO_2	1.28	0.38	0.37	1.12	[38]
THs	TiO_2	3.04	0.75	0.50	1.17	[39]
THs	TiO_2-FeO(25%)	7.89	0.79	0.57	3.55	[39]
THs	TiO_2-FeO(50%)	2.49	0.74	0.50	0.92	[39]
Alpinia purpurata	TiO_2	0.49	0.53	0.40	0.65	[13]
Alstroemeria	TiO_2	2.04	0.39	0.29	1.74	[13]
Chrysanthemum violet	TiO_2	0.85	0.58	0.44	1.35	[12]
Alstroemeria	TiO_2-Fe_2O_3(10%)	2.48	0.59	0.39	3.54	[this work]
Chrysanthemum violet	TiO_2-Fe_2O_3(10%)	2.37	0.50	0.44	3.24	[this work]
Alstroemeria	TiO_2-Fe_2O_3(20%)	3.91	0.60	0.43	6.33	[this work]
Chrysanthemum violet	TiO_2-Fe_2O_3(20%)	2.71	0.60	0.52	5.25	[this work]
Alstroemeria	TiO_2-Fe_2O_3(30%)	3.48	0.60	0.44	5.74	[this work]
Chrysanthemum violet	TiO_2-Fe_2O_3(30%)	2.42	0.59	0.46	4.15	[this work]

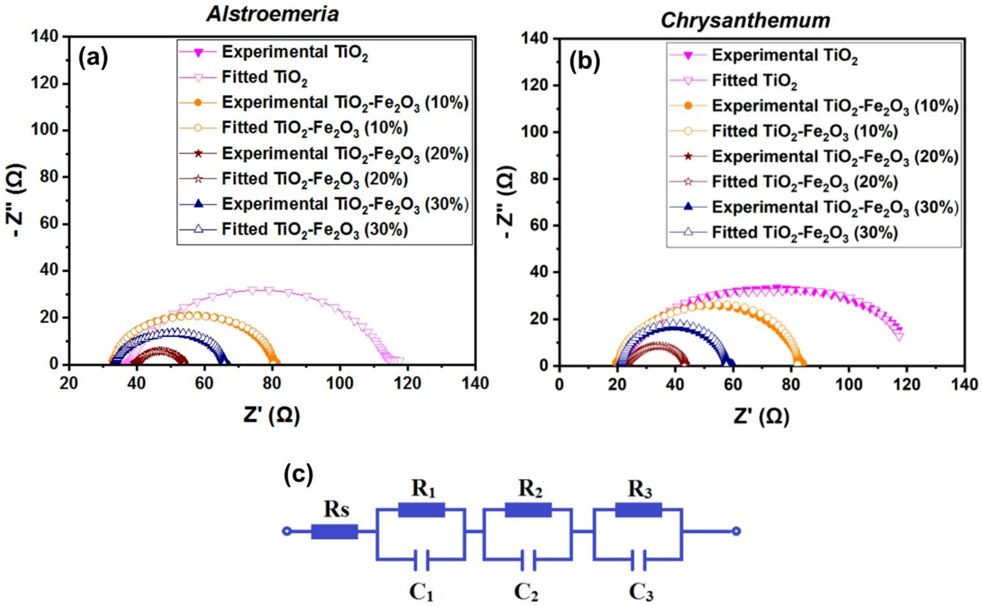

Fig. 9 EIS curves with various dopants: (**a**)*Alstroemeria*, (**b**) *Chrysanthemum* violet and (**c**) corresponding equivalent circuit

In addition to performance point of view, cost is a critical parameter when comparing DSSCs to conventional photovoltaic technologies. While silicon solar cells dominate the market due to their high efficiency, their fabrication involves capital and energy intensive processes, such as in got growth, wafer slicing, and vacuum deposition. By contrast, DSSCs can be produced at relatively low temperatures using simple deposition and sealing methods, which significantly reduces capital expenditure (CAPEX) per area. The use of natural dyes, such as anthocyanins extracted from *Alstroemeria* and *Chrysanthemum* petals, further decreases the material costs, as they can be obtained through straightforward ethanol-based extraction from abundant and renewable sources, including agricultural residues. This approach not only offers a renewable and eco-friendly alternative

Table 2 Values of each element of the equivalent circuit with their associated errors

Dyes/Semicondutor	$R_S(\Omega)$	$R_1(\Omega)$	$R_2(\Omega)$	$R_3(\Omega)$	$C_1(\mu F)$	$C_2(\mu F)$	$C_3(\mu F)$
Als: TiO_2	38.56 ±0.78	73.16 ±1.27	15.75 ±0.21	6.02 ±1.21	44.29 ±2.28	144.28 ±3.01	87.43 ±3.43
C.V.:TiO_2	31.51 ±0.35	47.85 ±3.04	43.65 ±3.15	7.099 ±7.24	812 ±7.14	142.5 ±3.02	92.42 ±5.44
Als: TiO_2-Fe_2O_3(10%)	33.18 ±0.26	24.60 ±11.36	22.44 ±12.5	8.49 ±5.93	47.30 ±18.24	18.80 ±6.41	73.49 ±6.15
C.V.:TiO_2-Fe_2O_3(10%)	55.43 ±0.24	44.27 ±3.19	17.56 ±8.08	3.91 ±9.74	46.57 ±6.25	27.12 ±3.38	78.26 ±7.47
Als: TiO_2-Fe_2O_3(20%)	39.29 ±0.13	2.67 ±13.20	10.20 ±3.22	1.68 ±4.46	16.19 ±23.92	10.41 ±1.79	45.36 ±7.56
C.V.:TiO_2-Fe_2O_3(20%)	83.32 ±0.10	16.57 ±1.45	3.26 ±7.22	2.25 ±0.13	12.16 ±3.31	78.74 ±7.26	48.82 ±9.30
Als: TiO_2-Fe_2O_3(30%)	33.67 ±0.29	22.90 ±3.30	9.20 ±8.11	7.84 ±0.29	34.07 ±6.41	19.33 ±3.56	64.46 ±13.47
C.V.:TiO_2-Fe_2O_3(30%)	21.60 ±0.58	36.01 ±0.69	12.38 ±11.43	9.14 ±0.57	16.54 ±1.55	23.67 ±20.10	68.53 ±15.17

Table 3 Stability results of the fabricated DSSCs

Dyes	Anode	Initial efficiency (%)	Final efficiency (%)	Time (months)	Efficiency Losses (%)
Alstroemeria	TiO_2-Fe_2O_3(10%)	3.54	3.02	6	2.64
Chrysanthemum violet	TiO_2-Fe_2O_3(10%)	3.24	2.97	6	1.44
Alstroemeria	TiO_2-Fe_2O_3(20%)	6.33	5.80	6	1.46
Chrysanthemum violet	TiO_2-Fe_2O_3(20%)	5.25	4.76	6	1.63
Alstroemeria	TiO_2-Fe_2O_3(30%)	5.74	5.21	6	1.61
Chrysanthemum violet	TiO_2-Fe_2O_3(30%)	4.15	3.82	6	1.38

to expensive ruthenium-based dyes but also enables potential scalability via roll-to-roll printing on flexible substrates. Therefore, DSSCs sensitized with natural dyes present a lower cost per functional area compared to silicon modules, especially for applications in indoor, portable, or IoT energy harvesting systems.

4 Conclusion

This study evaluated the impact of iron oxide (Fe_2O_3) doping on the photovoltaic performance of dye-sensitized solar cells (DSSCs) using titanium dioxide (TiO_2)-based photoanodes. Natural dyes extracted from *Alstroemeria* (Als) and *Chrysanthemum violet* (C.V.) served as eco-friendly photosensitizers. The experimental results demonstrated that optimal performance was achieved with 20% Fe_2O_3 doping, yielding the highest power outputs (Als: 1.01 mW/cm^2; C.V.: 0.84 mW/cm^2) and maximum conversion efficiency of 6.33% for the Als-based cell. Electrochemical characterization confirmed that Fe_2O_3 doping enhances solar energy conversion efficiency compared to mere TiO_2 cells. This improvement is attributed to enhanced light absorption in the visible spectrum, reduced electron-hole recombination, and improved dye-semiconductor interaction. Specifically, Fe_2O_3 doping introduces a broader absorption bandwidth and modifies the bandgap via Fermi level tuning, facilitating efficient charge separation and electron transport. However, a saturation effect was observed beyond 30% Fe_2O_3 doping, likely due to excessive thickening and reduced porosity of the photoanode layer, which hinders charge mobility and dye loading. Overall, the incorporation of Fe_2O_3 into TiO_2 photoanodes proved to be an effective strategy for significantly improving DSSC efficiency up to fourfold compared to the mere TiO_2 devices. These findings underscore the potential of Fe_2O_3-based composites DSSCs as a sustainable and cost-effective solution for solar energy harvesting.

Supplementary Information The online version contains supplementary material available at https://doi.org/10.1007/s00339-026-09332-5.

Acknowledgements Mr. H. O. da Cunha and Mr. A. M. B. Leite express their gratitude to the Coordenação de Aperfeiçoamento de Pessoal de Nível Superior (CAPES) (FUC-001) for providing financial support for their doctoral degrees. Dr. R. Suresh Babu would like to thank FAPERJ for the financial support of post-doctoral senior fellowship (E-26/203.465/2023 (293937). Prof. A L F de Barros acknowledge the Brazilian organizations CAPES, CNPq (Bolsa de Produtividade 30.7418/2021-9), FINEP (1455/24) and FAPERJ (E-26/201.801/2021, E-26-210.965/2021, E-26-210.801/2021, E-26-200.320/2023, E-26/202.601/2023, E-26/201.622/2023 and E-26/203.465/2023). The authors gratefully acknowledge Dr. P.S. Ramesh for his valuable support in XRD analysis, data interpretation, and crystal structure visualization using VESTA software.

Author contributions Conceptualization, methodology and writing—original draft preparation H.O.C.; software and validation, A.M.B.L.;

investigation, software, P.S.R.; formal analysis, reviewing and editing, R.S.B.; software and formal analysis, A.K.; reviewing and editing, supervision and funding acquisition, A.L.F.B.

Funding The Article Processing Charge (APC) for the publication of this research was funded by the Coordenação de Aperfeiçoamento de Pessoal de Nível Superior - Brasil (CAPES) (ROR identifier: 00x0ma614).

Data availability Not Applicable.

Declarations

Conflict of interests The authors declare no conflicts of interest.

References

1. O.A. Adelekan, B.S. Ilugbusi, O. Adisa, O.C. Obi, K.F. Awonuga, O.F. Asuzu, N.L. Ndubuisi, Energy transition policies: a global review of shifts towards renewable sources. Eng. Sci. Technol. J. **5**, 272–287 (2024). https://doi.org/10.51594/estj.v5i2.752
2. A. Triyanto, A. Nora'aini, S. Hasiah, S. Jan, I.Y. Norhafiza, Development of natural dye photosensitizers for dye-sensitized solar cells: a review. Environ. Sci. Pollut Res. **31**, 31679–31690 (2024). https://doi.org/10.1007/s11356-024-33360-4
3. A.U. Hassan, S.H. Sumrra, M. Zubair, G. Mustafa, M.F. Nazar, M.N. Zafar, Structurally modulated D-π-D-A(Semiconductor) anchoring dyes to enhance the tunable NLO response: a DFT/TDDFT quest for new photovoltaic materials. Struct. Chem. **34**, 1043–1060 (2023). https://doi.org/10.1007/s11224-022-02070-3
4. S. Xu, P. Huang, W. Zhong, Y. Luo, H. Fu, Z. Xiao, H. Jin, Y. Liu, Renewable flower-based dye-sensitized solar cells using natural dye and natural carbon counter electrode. Energy Adv. **4**, 947–957 (2025). https://doi.org/10.1039/D5YA00086F
5. A.S. Najm, S.A. Alwash, N.H. Sulaiman, M.S. Chowdhury, K. Techato, Environ. Prog. Sustain. Energy **42**(1), e13955 (2023). https://doi.org/10.1002/ep.13955
6. M. Mahmoudi, A. Alizadeh, M. Roudgar-Amoli, Z. Shariatinia, Spectrochim. Acta A Mol. Biomol. Spectrosc. **289**, 122214 (2023). https://doi.org/10.1016/j.saa.2022.122214
7. C. Nizamudeen, R. Krishnapriya, M.S. Mozumder, A.-H.I. Mourad, T. Ramachandran, Photovoltaic performance of MOF-derived transition metal doped titania-based photoanodes for DSSCs. Sci. Rep. **13**, 6345 (2023). https://doi.org/10.1038/s41598-023-33565-6
8. F. Rehman, N. Alam, M. Sohail, M. Ahmad, M.I. Siddiqui, M.I. Irshad, A. Mumtaz, J. Photochem. Photobiol. A Chem. **444**, 114956 (2023). https://doi.org/10.1016/j.jphotochem.2023.114956
9. M. Abdullaev, A. Althomali, M. Alshahrani, M. Alshahrani, M. Alshahrani, Enhancing dye-sensitized solar cell performance by employing an innovative WSe_2:Zn counter electrode for improved electrocatalytic activity. Mater. Sci. Semicond. Process. **171**, 108015 (2023). https://doi.org/10.1016/j.mssp.2023.108015
10. V. Gayathri, A. Muthukumar, C.R. Mohan, GQDs assisted $Ba_6Co_{25}S_{27}$/MWCNT composite as a promising candidate for supercapacitor and a perspective Pt-free counter electrode in DSSC for enhancing the short circuit current. Colloids Surf. A Physicochem. Eng. Asp. **683**, 132973 (2024). https://doi.org/10.1016/j.colsurfa.2023.132973
11. J. Barichello, P. Mariani, L. Vesce, D. Spadaro, I. Citro, F. Matteocci, A. Bartolotta, A. Di Carlo, G. Calogero, Bifacial dye-sensitized solar cells for indoor and outdoor renewable energy-based application. J. Mater. Chem. C **12**, 2317–2349 (2024). https://doi.org/10.1039/D3TC03220E
12. A.M.B. Leite, J.A.F.C.R. Rodrigues, R.S. Babu, A.L.F. de Barros, Construction and characterization of organic photovoltaic cells sensitized by Chrysanthemum-based natural dye. Spectrochim. Acta A Mol. Biomol. Spectrosc. **284**, 121780 (2023). https://doi.org/10.1016/j.saa.2022.121780
13. L.R.B. da Conceição, H.O. da Cunha, A.M.B. Leite, R.S. Babu, S. Raja, C. Ribeiro, A.L.F. de Barros, Evaluation of solar conversion efficiency in dye-sensitized solar cells using natural dyes extracted from Alpinia purpurata and Alstroemeria flower petals as novel photosensitizers. Colorants **2**, 618–631 (2023). https://doi.org/10.3390/colorants2040032
14. L.R.B. da Conceição, H.O. da Cunha, A.M.B. Leite, J.A.F.C.R. Rodrigues, R.S. Babu, A.L.F. de Barros, Investigation of nanostructured TiO_2 thin film coatings for DSSCs application using natural dye. Optik **300**, 171635 (2024). https://doi.org/10.1016/j.ijleo.2024.171635
15. B.C. Ferreira, R.S. Babu, L.R.B. da Conceição, H.O. da Cunha, D.M. Sampaio, L.M. Samyn, A.L.F. de Barros, Performance evaluation of DSSCs using naturally extracted dyes from petals of *Lantana repens* and *Solidago canadensis* flowers as light-harvesting units. Ionics **28**, 5233–5242 (2022). https://doi.org/10.1007/s11581-022-04727-9
16. F.M.M. dos Santos, A.M.B. Leite, L.R.B. da Conceição, Y. Sasikumar, R. Atchudan, M.F. Pinto, R.S. Babu, A.L.F. de Barros, Effect of bandgap energies by various color petals of *Gerbera jamesonii* flower dyes as a photosensitizer on enhancing the efficiency of dye-sensitized solar cells. J. Mater. Sci. Mater. Electron. **33**, 20338–20352 (2022). https://doi.org/10.1007/s10854-022-08849-8
17. F.C. Ferreira, R.S. Babu, A.L.F. de Barros, S. Raja, L.R.B. da Conceição, L.H.C. Mattoso, Photoelectric performance evaluation of DSSCs using the dye extracted from different color petals of *Leucanthemum vulgare* flowers as novel sensitizers. Spectrochim. Acta Part A Mol. Biomol. Spectrosc. **233**, 118198 (2020). https://doi.org/10.1016/j.saa.2020.118198
18. G.A. Alamu, P.S. Ayanlola, K.K. Babalola, O. Adedokun, Y.K. Sanusi, G.R. Fajinmi, Green synthesis and characterizations of magnetic iron oxide nanoparticles using *Moringa oleifera* extract for improved performance in dye-sensitized solar cell. Chem. Phys. Impact **8**, 100542 (2024). https://doi.org/10.1016/j.chphi.2024.100542
19. S. Huang, J. Shen, Y. Wu, X. Li, Y. Ma, Y. Xie, C. Yu, Y. Zhang, J. Zhang, $Bi_2O_2CO_3$ co-catalyst modification BiOBr driving efficient photoreduction CO_2. Colloids Surf. A, Physicochem. Eng. Asp. **725**, 137731 (2025). https://doi.org/10.1016/j.colsurfa.2025.137731
20. N. Ahmadi, R. Yeganeh, M. Valizadeh, T. Valadbeigi, Improvement of the fill factor characteristic of TiO_2-based dye-sensitive solar cell using lichen *Collema nigra*. Opt. Mater. **131**, 112638 (2022). https://doi.org/10.1016/j.optmat.2022.112638

21. G.N. Arka, S.B. Prasad, S.C. Singh, Comprehensive study on dye sensitized solar cell in subsystem level to excel performance potential: a review. Sol. Energy **226**, 192–213 (2021). https://doi.org/10.1016/j.solener.2021.08.037
22. N. Wetchakun, B. Incessungvorn, K. Wetchakun, S. Phanichphant, Influence of calcination temperature on anatase to rutile phase transformation in TiO_2 nanoparticles synthesized by the modified sol–gel method. Mater. Lett. **82**, 195–198 (2012). https://doi.org/10.1016/j.matlet.2012.05.092
23. H.A. Mahmoud, K. Narasimharao, T.T. Ali, K.M.S. Khalil, Acidic peptizing agent effect on anatase-rutile ratio and photocatalytic performance of TiO_2 nanoparticles. Nanoscale Res. Lett. **13**, 48 (2018). https://doi.org/10.1186/s11671-018-2465-x
24. H. Mansour, H. Letifi, R. Bargougui, S.D. Almeida-Didry, B. Negulescu, C. Autret-Lambert, A. Gadri, S. Ammar, Appl. Phys. A **123**, 787 (2017). https://doi.org/10.1007/s00339-017-1408-1
25. M. Hjiri, Highly sensitive NO_2 gas sensor based on hematite nanoparticles synthesized by sol–gel technique. J. Mater. Sci. Mater. Electron. **31**, 5025–5031 (2020). https://doi.org/10.1007/s10854-020-03069-4
26. C. Cao, C. Hu, W. Shen, S. Wang, S. Song, M. Wang, Improving photoelectrochemical performance by building Fe_2O_3 heterostructure on TiO_2 nanorod arrays. Mater. Res. Bull. **70**, 155–162 (2015). https://doi.org/10.1016/j.materresbull.2015.04.036
27. Q. Mei, F. Zhang, N. Wang, Y. Yang, W. Wang, TiO_2/Fe_2O_3 heterostructures with enhanced photocatalytic reduction of Cr(VI) under visible light irradiation. RSC Adv. **9**, 22764–22771 (2019). https://doi.org/10.1039/c9ra03531a
28. M. Sakar, R.M. Prakash, T.-O. Do, Insights into the TiO<Subscript>2</Subscript>-based photocatalytic systems and their mechanisms. Catalysts **9**, 680 (2019). https://doi.org/10.3390/catal9080680
29. P. Dhamodharan, J. Chen, C. Manoharan, Fabrication of In doped ZnO thin films by spray pyrolysis as photoanode in DSSCs. Surfaces and Interfaces **23**, 100965 (2021). https://doi.org/10.1016/j.surfin.2021.100965
30. U. Mahajan, K. Prajapat, M. Dhonde, K. Sahu, P.M. Shirage, Natural dyes for dye-sensitized solar cells (DSSCs): an overview of extraction, characterization and performance. Nano-Structures & Nano-Objects **37**, 101111 (2024). https://doi.org/10.1016/j.nanoso.2024.101111
31. A. Manimekalai, R. Parimaladevi, M. Umadevi, Enriched In_2O_3/WO_3 nanocomposites as photoanode for a dye-sensitized solar cell in photo powered energy system. Mater. Lett. **319**, 132285 (2022). https://doi.org/10.1016/j.matlet.2022.132285
32. G.K. Karaoğlan, A. Hışır, Y.E. Maden, M.Ö. Karakuş, A. Koca, Synthesis, characterization, electrochemical, spectroelectrochemical properties, and dye-sensitized solar cell performance of phthalocyanines containing carboxylic acid anchoring groups as photosensitizers. Dyes Pigm. **204**, 110390 (2022). https://doi.org/10.1016/j.dyepig.2022.110390
33. S. Venkatesan, Y.Y. Chen, H. Teng, Y.L. Lee, Enhanced adsorption on TiO_2 photoelectrodes of dye-sensitized solar cells by electrochemical methods dye. J. Alloys Compd. **903**, 163959 (2022). https://doi.org/10.1016/j.jallcom.2022.163959
34. J. Conradie, Effective dyes for DSSCs–important experimental and calculated parameters. Energy Nexus **13**, 100282 (2024). https://doi.org/10.1016/j.nexus.2024.100282
35. Y. Kumar, T. Chhalodia, P.K.G. Bedi, P.L. Meena, Photoanode modified with nanostructures for efficiency enhancement in DSSC: a review. Carbon Lett. **33**, 35–58 (2023). https://doi.org/10.1007/s42823-022-00422-x
36. A. Agrawal, S.A. Siddiqui, A.K. Soni, G.D. Sharma, Advancements, frontiers and analysis of metal oxide semiconductor, dye, electrolyte and counter electrode of dye-sensitized solar cell. Sol Energy. **231**, 16–30 (2022). https://doi.org/10.1016/j.solener.2022.01.027
37. F. Job, S. Mathew, R. Rajendran, T. Meyer, S. Narbey, An investigation on the performance of dye-sensitized solar cell at various light intensities. Mater. Today Proc. **43**, 3386–3390 (2021). https://doi.org/10.1016/j.matpr.2020.08.372
38. S.M. Amir-Al Zumahi, N. Arobi, M.M. Rahman, M.K. Hossain, M.A.J. Rozy, M.S. Bashar, A. Amri, H. Kabir, M.A. Hossain, F. Ahmed, Understanding the optical behaviours and the power conversion efficiency of novel organic dye and nanostructured TiO_2 based integrated DSSCs. Sol Energy. **226**, 267–276 (2021). https://doi.org/10.1016/j.solener.2021.07.024
39. S. Rudra, H.-S. Seo, S. Sarker, D.M. Kim, Simulation and electrochemical impedance spectroscopy of dye-sensitized solar cells. J. Indus Eng. Chem. **97**, 574–583 (2021). https://doi.org/10.1016/j.jiec.2021.03.010
40. A. Daoud, A. Cheknane, A. Meftah, J.-M. Nunzi, M. Shalabi, H.S. Hilal, Spatial separation strategies to control charge recombination and dye regeneration in p-type dye sensitized solar cells. Solar Energy **236**, 107–152 (2022). https://doi.org/10.1016/j.solener.2022.02.050
41. L. Yu, Z. Li, Mater. Sci. Semicond. Process. **149**, 106881 (2022). https://doi.org/10.1016/j.mssp.2022.106881
42. A.J.A. Abiodun, G.A. Alamu, O. Adedokun, O.O. Daramola, Y.K. Sanusi, Iron oxide green synthesized nanoparticles for improved performance in monolithic dye sensitized solar cells. LAUTECH J. Eng. Technol. **18**, 128–137 (2024). https://doi.org/10.36108/laujet/4202.81.0221
43. H.O. da Cunha, A.M.B. Leite, P.S. Ramesh, R.S. Babu, A.L.F. de Barros, Improved solar cells efficiency with TiO_2/CuO nanocomposite as photoanode sensitized by natural dyes from scarlet eggplant, pitomba and black grapes. J. Mater. Sci. Mater. Electron. **36**, 35 (2025). https://doi.org/10.1007/s10854-024-14106-x
44. N. Kanjana, W. Maiaugree, P. Poolcharuansin, P. Laokul, Synthesis and characterization of Fe-doped TiO_2 hollow spheres for dye-sensitized solar cell applications. Materials Science and Engineering: B **271**, 115311 (2021). https://doi.org/10.1016/j.mseb.2021.115311